ACS APPLIED MATERIALS & INTERFACES

Research Article

www.acsami.org

Core–Shell Prussian Blue Analogue Molecular Magnet $Mn_{1.5}[Cr(CN)_6]\cdot mH_2O@Ni_{1.5}[Cr(CN)_6]\cdot nH_2O$ for Hydrogen Storage

Pramod Bhatt,*[,†] Seemita Banerjee,[‡] Sharmistha Anwar,[§] Mayuresh D. Mukadam,[†] Sher Singh Meena,[†] and Seikh M. Yusuf*[,†]

[†]Solid State Physics Division and [‡]Chemistry Division, Bhabha Atomic Research Centre, Mumbai 400085, India

[§]Colloids & Materials Chemistry, CSIR-Institute of Minerals and Materials Technology, Bhubaneswar 751013, India

ABSTRACT: Core–shell Prussian blue analogue molecular magnet $Mn_{1.5}[Cr(CN)_6]\cdot mH_2O@Ni_{1.5}[Cr(CN)_6]\cdot nH_2O$ has been synthesized using a core of $Mn_{1.5}[Cr(CN)_6]\cdot 7.5H_2O$, surrounded by a shell of $Ni_{1.5}[Cr(CN)_6]\cdot 7.5H_2O$ compound. A transmission electron microscopy (TEM) study confirms the core–shell nature of the nanoparticles with an average size of ~25 nm. The core–shell nanoparticles are investigated by using x–ray diffraction (XRD), energy-dispersive X-ray spectroscopy (EDS) and elemental mapping, X-ray photoelectron spectroscopy (XPS), thermogravimetric analysis (TGA), and infrared (IR) spectroscopy. The Rietveld refinement of the XRD pattern reveals that the core–shell compound has a face–centered cubic crystal structure with space group *Fm3m*. The observation of characteristic absorption bands in the range of 2000–2300 cm^{-1} in IR spectra corresponds to the CN stretching frequency of $Mn^{II}/Ni^{II}–N\equiv C–Cr^{III}$ sequence, confirming the formation of Prussian blue analogues. Hydrogen absorption isotherm measurements have been used to investigate the kinetics of molecular hydrogen adsorption into core–shell compounds of the Prussian blue analogue at low temperature conditions. Interestingly, the core–shell compound shows an enhancement in the hydrogen capacity (2.0 wt % at 123 K) as compared to bare–core and bare–shell compounds. The hydrogen adsorption capacity has been correlated with the specific surface area and TGA analysis of the core–shell compound. To the best of our knowledge, this is the first report on the hydrogen storage properties of core–shell Prussian blue analogue molecular magnet that could be useful for hydrogen storage applications.

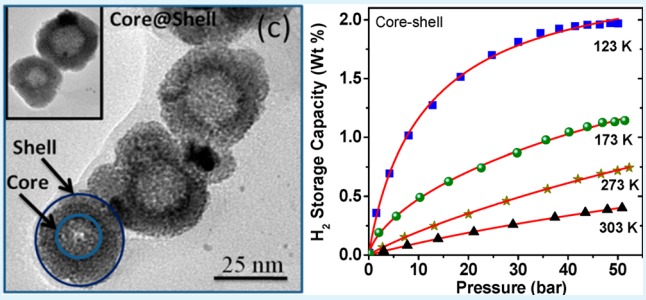

KEYWORDS: *Prussian blue analogues, hydrogen storage, core–shell nanostructure, molecular magnets, Rietveld refinement, transmission electron microscopy*

INTRODUCTION

Prussian blue analogues (PBAs) form a unique class of materials which have received a great attention recently because of their multifunctional properties, such as photomagnetism,[1,2] piezomagnetism,[3] magnetic pole inversion,[4,5] zero/negative thermal expansion,[6] and possible wide technological applications of hydrogen storage,[7] magneto–optical switching,[8] batteries materials (as cathode),[9,10] ion exchange for the removal of Cs-137,[11] ion sensing,[12,13] and electro- and photocatalysis.[14] Among all possible technological applications, hydrogen storage ability of PBAs is of great importance, because today hydrogen is considered as an alternative fuel for environmentally friendly energy technology because of its clean combustion and high heating value. However, effective methods for hydrogen storage are still challenging. Though, various materials such as alloys, metal hydrides, chemical hydrides, nanostructure carbon, porous frameworks, and organic/molecular compound have already been demonstrated for hydrogen storage applications,[15−21] the extensive efforts have been still directed toward enhancing the storage capacity of hydrogen by modifying or synthesizing new materials, and by introducing new synthesis strategies. We have synthesized core–shell structure of PBAs to improve the hydrogen storage properties of the PBA compounds. The core–shell structure of PBAs shows many interesting properties due to their different chemical nature of the core, shell and their interface. For example, the redox stability can be enhanced by enclosing the high–capacity PBAs in a core–shell structure with a robust shell in a well-characterized NiFe-based PBA.[22] In another example, core–shell structure of PBAs has been synthesized for enhancing the coexistence of both high capacity and good stability as a cathode material for Ni-rich $Li[Ni_{1-x}M_x]O_2$.[22,23] Moreover, charge–transfer induced spin transition switching properties of core–shell structures consisting of a photo–switchable core with a $Rb_{0.2}Ni[Cr(CN)_6]_{0.7}\cdot zH_2O$ ferromagnetic shell have also been studied.[24] Core–shell nanoparticles consisting of two different PBAs, one with a high capacity core and the other with lower capacity but highly stable shell, can provide an enhanced rate capability as cathode materials in sodium–ion batteries.[25] The enhanced cyclability as lithium ion

Received: June 4, 2014
Accepted: October 2, 2014
Published: October 2, 2014

cathode materials has been obtained using the core−shell nanoparticles of bimetallic cyanide-bridged coordination polymers.[22] Similarly, core−shell PBAs of $K_jNi_k[Cr(CN)_6]_l \cdot nH_2O$ as core with $Rb_aCo_b[Fe(CN)_6]_c \cdot mH_2O$ as shell have been synthesized for the purpose of studying a persistent photoinduced magnetization in the core−shell heterostructures.[26] However, the hydrogen storage property of core−shell structure of PBAs has not been studied until now in spite of a better chemical reactivity of a core−shell structure. Recently, a core−shell strategy has been used for high reversible hydrogen storage capacity in $NaBH_4$ compound.[18,27] By using a metal forming a borohydride of lower stability than $NaBH_4$, hydrogen kinetics could be enhanced by the unstable borohydride shell pumping hydrogen in/out of the structure.[18,27] Following this, we have, therefore, synthesized a core−shell structure of PBAs for investigation of its hydrogen storage properties.

The hydrogen storage properties of bare PBAs (i.e., without any core−shell structure) have been previously investigated. The presence of vacancies and interstitial sites offers an ideal platform for storage of hydrogen in such compounds. The first study on hydrogen storage properties for dehydrated PBAs of the type $M_3[Co(CN)_6]_2$ (M = Mn, Fe, Co, Ni, Cu, and Zn) was reported by Kaye et al. wherein it was observed that the interactions with bridging cyanide ligands and/or coordinatively unsaturated metal centers are responsible for higher adsorption enthalpies.[7] The maximum hydrogen storage of 1.8 wt % was reported for $Cu_3[Co(CN)_6]_2$ at 77 K.[7] Followed by this work, investigation of hydrogen storage in other PBAs has been continuously accelerated. The role of different building blocks in zeolite-like Zn based hexacyanometallates, $Zn_3A_2[M(CN)_6]_2$ with A = K, Rb, and Cs, and M = Fe, Ru, and Os was investigated for their hydrogen storage properties, and estimated values for the adsorption heats follow the order: Os > Ru > Fe.[28] Similarly, hydrogen storage in various copper based Prussian blue analogues was investigated, and the maximum hydrogen storage of 2.61 wt % was reported for $Cu_3[Co(CN)_6]_2$ at 75 K.[29] The Cu-based PBAs are known to have higher affinities for H_2 because of increased π-back bonding into the H_2 σ^* orbital. Generally H_2 storage in PBAs is dominated by the electrostatic interaction between the cavity electric field gradient and the quadrupole moment of the guest molecule.[30,31] However, the larger excess of H_2 for copper-based Prussian blue analogues depends upon the composition. The additional interaction, which determines the large H_2 storage capacity in copper-based PBAs, is related to the electronic state of copper atom in this family of compounds, particularly to its large electron density.[29] Apart from the building blocks, the role of vacancies also affects the hydrogen storage properties of PBAs.[32] Hydrogen storage properties of the dehydrated Prussian blue type solids $Ga[Co(CN)_6]$, $Fe_4[Fe(CN)_6]_3$, $M_2[Fe(CN)_6]$ (M = Mn, Co, Ni, and Cu), and $Co_3[Co(CN)_5]_2$ were compared to those of $M_3[Co(CN)_6]_2$ (M = Mn, Fe, Co, Ni, Cu, and Zn) in the literature. Hydrogen adsorption isotherms, measured at 77 K, revealed a correlation between uptake capacity and the concentration of framework vacancies, with 1.4 wt % for $Ga[Co(CN)_6]$, 1.6 wt % for $Fe_4[Fe(CN)_6]_3$, 2.1 wt % for $Cu_3[Co(CN)_6]_2$, and 2.3 wt % for $Cu_2[Fe(CN)_6]$.[32] Hydrogen storage in the iron series of porous Prussian blue analogues $T_3[Fe(CN)_6]_2$ with T = Mn, Co, Ni, Cu, Zn, and Cd was also studied, and maximum hydrogen sorption of 2.33 wt % was reported for $Mn_3[Fe(CN)_6]_2$ compound at liquid nitrogen temperature.[33] In addition, nanoporous Prussian blue analogues, $M^{II}_3[Co^{III}(CN)_6]_2$ (M^{II} = Mn, Fe, Co, Ni, Cu, Zn, and Cd), which contain coordinatively unsaturated divalent metal cations, were investigated for hydrogen storage properties with maximum reversible sorption of hydrogen gas up to 1.2 wt % at 77 K.[19] Moreover, dehydrated variants for hydrogen adsorption of the cyano-bridged framework compounds $A_2Zn_3[Fe(CN)_6]_2.xH_2O$ (A = H, Li, Na, K, Rb) were studied, revealing maximum H_2 adsorption properties of 1.4 wt %.[34] The role of the exchangeable alkali metal ion for hydrogen storage in porous cyanometalates $Zn_3A_2[Fe(CN)_6]_2$ where A = Na^+, K^+, Rb^+, and Cs^+ was reported. The alkali metal modulates the electric field gradient within the pores, and thereby also the guest−host interaction for the hydrogen molecule adsorption.[30] Reversibility of H_2 adsorption into the PBAs $Cu_3[Co(CN)_6]_2$ films was also investigated for hydrogen storage, and found that adsorption rate substantially decreases with the decreasing thickness of the films.[35] Though, different forms of PBAs compounds have been synthesized for hydrogen storage properties, core−shell structure of PBAs has not been yet reported and the present study forms the first report on the hydrogen storage properties of any core−shell structure of PBAs.

EXPERIMENTAL SECTION

The polycrystalline samples of bare−core $\{Mn_{1.5}[Cr(CN)_6]\cdot 7.5H_2O\}$, bare−shell $\{Ni_{1.5}[Cr(CN)_6]\cdot 7.5H_2O\}$, and core−shell $\{Mn_{1.5}[Cr(CN)_6]\cdot mH_2O@Ni_{1.5}[Cr(CN)_6]\cdot nH_2O\}$ compounds are separately prepared using the co−precipitation method.[36] The chemicals $\{Mn(II)Cl_2.4H_2O$, $Ni(II)(NO_3)_2\cdot 6H_2O$ and $K_3[Cr(CN)_6]\}$ were reagent grade, and used as received from Sigma−Aldrich. For the synthesis of the bare−core $Mn_{1.5}[Cr(CN)_6]\cdot 7.5H_2O$, the required amounts of 0.15 Mol. and 0.1 Mol. aqueous solutions (10 mL each) of $MnCl_2$ and $K_3[Cr(CN)_6]$, respectively, were prepared and heated separately up to 40 °C for 15 min. The prepared $MnCl_2$ solution is thereafter mixed with the rapidly stirred aqueous solution of $K_3[Cr(CN)_6]$, and heated up to 60 °C for 15 min. The precipitate of bare−core compound is formed. The precipitate is filtered, and washed many times with doubly distilled water and ethanol, and finally allowed to dry in air. Similarly, the bare−shell compound $Ni_{1.5}[Cr(CN)_6]\cdot 7.5H_2O$ is separately synthesized by mixing of $Ni(II)(NO_3)_2\cdot 6H_2O$ and $K_3[Cr(CN)_6]$ chemicals, similar to the method as described above for the bare−core compound. However, in order to synthesize the core−shell compound, 5 mL of the precipitated solution of bare−core compound $Mn_{1.5}[Cr(CN)_6]\cdot 7.5H_2O$, is diluted in 20 mL of $K_3[Cr(CN)_6]$ solution. For producing the core−shell structures, we have adopted the method as reported in the literature.[22,24,26] However, the core−shell structure of PBAs was initially reported by the Catala et al.[37] The particles were subsequently filtered before being washed with an ultrapure water, and redispersed in 100 mL of water for use in the next step. Then the core−shell, $Mn_{1.5}[Cr(CN)_6]\cdot mH_2O@Ni_{1.5}[Cr(CN)_6]\cdot nH_2O$ compound was subsequently grown by simultaneous and dropwise addition (0.50 mL/min) of $Ni(II)(NO_3)_2\cdot 6H_2O$ (0.15 M, 10 mL) and $K_3[Cr(CN)_6]$ (0.1 M, 10 mL) solutions to the diluted core solution. The solutions were kept under vigorous stirring at 20 °C during the mixing, and for 1 h after all additions were completed. The precipitate was filtered, and washed many times with doubly distilled water and finally allowed to dry in air.

The chemical composition (in wt %) obtained from elemental analysis for the bare−core, bare−shell, and core−shell compounds are as follows. (i) Bare−core: formula $Mn_{1.5}[Cr(CN)_6]\cdot 7.5H_2O$ Mn, 24.2; Cr, 16.0; C, 22.5; N, 24.1; and calculated Mn, 23.0; Cr, 14.5; C, 20.1; N, 23.4. (ii) Bare−shell: formula $Ni_{1.5}[Cr(CN)_6]\cdot 7.5H_2O$ Ni, 25.2; Cr, 15.9; C, 18.8; N, 23.0 and calculated Ni: 24.2, Cr: 14.2, C: 19.8, N: 23.1; (iii) core−shell compound, $Mn_{1.5}[Cr(CN)_6]\cdot mH_2O@$ $Ni_{1.5}[Cr(CN)_6]\cdot nH_2O$, Mn: 12.1, Ni:10.2, Cr: 13.8, C: 21.5, N: 25.2 calculated Mn: 11.5, Ni:8.1, Cr: 14.5, C: 20.1, N: 23.4.

Transmission electron microscopy (TEM) has been performed at an operating voltage of 200 kV using FEI, Model Tecnai 30 STG[2] Philips Amsterdam, Netherland after ultrasonically dispersing the core−shell compound in water. Images were recorded in the low-dose mode in order to avoid sample damage caused by electron beam.

The X-ray diffraction (XRD) measurements of all compounds were performed at room temperature in a Bragg−Brentano geometry using a Rigaku diffractometer over an angular (2θ) range of 10−60° in equal 2θ steps of 0.02° using a Cu−K_α (λ = 1.54 Å) radiation. A detailed structural analysis is performed on the XRD data by the Rietveld refinement method with the Fullprof program.[38]

The energy-dispersive X-ray spectroscopy (EDS) and elemental analysis has been done using VEGA microscope (TESCAN). The X-ray photoelectron spectroscopy for the core−shell compound has been carried out using Al K-α source (1446.6 eV) at ultra high vacuum conditions of 1×10^{-9} mbar.

The infrared (IR) spectra were recorded in the range of 400−4000 cm^{-1} by loading the samples in a KBr pellet on a Bruker VERTEX 80v Fourier transform infrared (FTIR) spectrometer.

Thermogravimetric analysis (TGA) and Differential thermal analysis (DTA) measurements were carried out using Mettler thermogravimetric analyzer (TG 50). The thermograms are recorded in nitrogen atmosphere at a heating rate of 5 °C min^{-1} in the temperature range 40−750 °C.

The hydrogen adsorption isotherms were recorded at different temperatures using an IMI analyzer (from Hiden Isochema, UK). The sample with known weight was loaded in the sample holder and sealed using a metallic gasket. Before the hydrogen adsorption isotherm, pycnometric measurement was done to correct for the sample volume. The hydrogen adsorption data, using an optimal measurement time, were obtained with a sample of about 250 mg. Prior to recording adsorption isotherms, the samples were degassed under turbo vacuum at a temperature of 80 °C with a heating rate of 5 °C/min. The isothermal measurements up to a hydrogen pressure of 50 atm were carried out at different temperatures of 300, 273, 173, and 123 K.

RESULTS AND DISCUSSION

The TEM images of the bare−core, bare−shell and core−shell compounds are shown in Figure 1a−c, respectively. The images

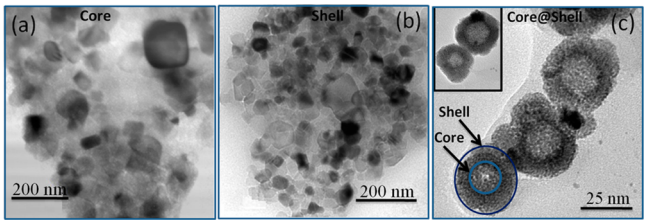

Figure 1. TEM image of the (a) bare−core, (b) bare−shell, and (c) core−shell nanoparticles. Inset of figure c shows the variation in the core size of the particles. The core−shell particle has been outlined by the circle in order to visualize better way.

show the particles are uniformly distributed for all the compounds. The shape of the particles for bare−core (a) compound is found to be rectangular whereas for the case of bare−shell (b) compound, it is found to be spherical. TEM image of the core−shell compound $Mn_{1.5}[Cr(CN)_6]\cdot mH_2O$@ $Ni_{1.5}[Cr(CN)_6]\cdot nH_2O$ is shown in Figure 1c. The figure shows the contrast between the core and shell counterparts, confirming the core−shell nature of the particles. The particles are found to be spherical in shape with size distribution of ~25−30 nm. The TEM study reveals the nanoparticle nature of the core−shell compound with the diameter of the core ~15 nm and shell thickness ~5 nm as marked in Figure 1c. It is noted that the core−shell compound exhibits slight variation in their respective core and shell sizes, however, TEM image ruled out the presence of any uncovered cores or side nucleation of core−shell compound. It should be noted that the size and nucleation of the core−shell particles are not controllable in the present study. However, the core−shell heterostructures of PBAs with controlled particle size have also been previously synthesized by Presle et al.[24] They have shown that the size distribution could be subsequently reduced by varying differential centrifugation speed. Moreover, another study by Catala and co−workers showed that the nucleation could be prevented by the control of the addition rate and of the concentration of the shell reactants.[37]

Figure 2 presents room temperature XRD patterns of the bare−core, bare−shell, and core−shell compounds. All the

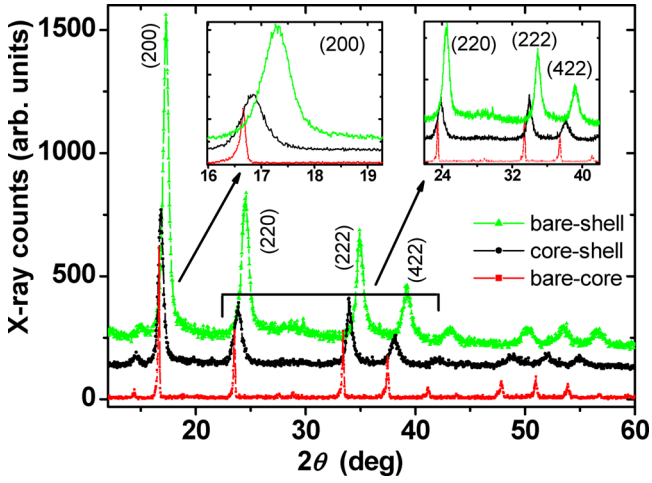

Figure 2. Room-temperature XRD patterns of bare−core, bare−shell, and core−shell compounds. Right and left side insets show the magnified view of the XRD patterns for better visibility.

patterns show crystalline nature of the compounds. It is clearly seen for the core−shell compound that, the intensity of the Bragg peaks decreases and width of the peaks becomes broad compared to those for the bare−core and bare−shell compounds. The nanocrystalline nature of the bare-core, bare-shell, and core−shell compounds is evident. In addition, the Bragg peaks for the core−shell compound shift to higher 2θ side with respect to both bare−core and bare−shell compounds. The XRD-derived particle size was found to be 76, 17, and 15 nm for the bare−core, bare−shell, and core−shell compounds, respectively. The TEM study also supports the nano sized formation of core−shell compound. The variation in the particle size derived from XRD and TEM could be different due to the fact that these two techniques have different method of particle size measurement and working principles. The particle size derived from the XRD is based on the Scherrer formula and has indirect estimations of the particle size using only intense Bragg peak, whereas the TEM has a direct method of measuring particle size with information in a real space. Therefore, the estimated particle size of core−shell compound is different using the XRD and TEM techniques.

Figure 3 presents the Rietveld refined[39] (using the FULLPROF program[38]) room temperature x−ray powder diffraction patterns of (a) the bare−core, (b) core−shell, and (c) bare−shell compounds. It is evident from the derived results of the fitted XRD patterns that the bare−core, and

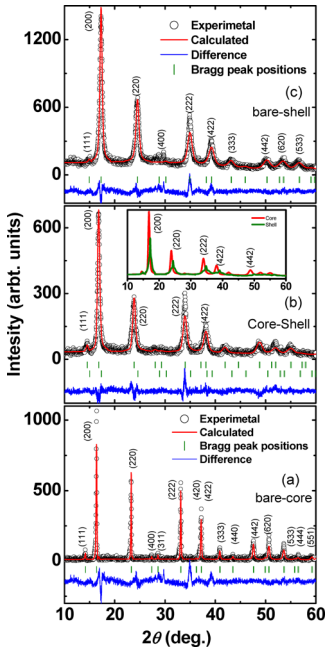

Figure 3. Rietveld refined room-temperature XRD patterns of (a) bare−core, (b) core−shell, and (c) bare−shell compounds. Open circles and solid lines indicate the observed and the calculated patterns, respectively. Solid lines at the bottom show the difference between observed and calculated patterns. Vertical lines at the bottom of XRD patterns show the position of allowed Bragg peaks, and their corresponding (*hkl*) values are also marked for the compounds. Inset of b shows the core and shell phase contribution in the fitting of the core−shell compound.

bare−shell compounds are in single-crystalline phase. The structure of the all compounds is a face centered cubic (fcc) with the space group *Fm*3*m*. The lattice constants are found to be ∼10.80 (5) and 10.26 (6) Å for the bare−core, $Mn_{1.5}[Cr(CN)_6]\cdot 7.5H_2O$ and bare−shell, $Ni_{1.5}[Cr(CN)_6]\cdot 7.5H_2O$ compounds, respectively. As expected, the XRD pattern of the core−shell compound consists of the contribution from both the core and shell compounds as it is well fitted with the structural model of having contributions from two phases with space group *Fm*3*m*. The inset of Figure 3b shows the individual contributions of the bare−core and bare−shell in the core−shell compound. The lattice constant for core−shell compound, $Mn_{1.5}[Cr(CN)_6]\cdot mH_2O@Ni_{1.5}[Cr(CN)_6]\cdot nH_2O$ is found to be ∼10.51(5) and 10.26(2) Å, respectively, for the two phases. The important structural parameters, such as atomic coordinates and site occupancies, derived from the Rietveld analysis, are shown in Table 1. The number of total water molecules is estimated from the derived number of oxygen atoms, obtained from the Rietveld refinement of the XRD patterns shown in Figure 3. It is estimated that the ∼33% $[Cr(CN)_6]$ vacancies present in both bare−core and bare−shell compounds result into two types of water molecules i.e. coordinated and noncoordinated. The coordinated water molecules reside at 24*e* crystallographic sites, and the noncoordinated water molecules reside at 8*c* and 32*f* interstitial sites. The schematic crystal structure of the core−shell compound is shown in Figure 4. The transition metal ions (Mn^{II} or Ni^{II}) are located at the 4*a* (0, 0, 0) crystallographic position, while the Cr^{III} ions occupy the 4*b*(1/2, 1/2, 1/2) crystallographic position. The C and N reside at 24*e*(*x*, 0, 0) sites which are partially occupied due to $[Cr(CN)_6]$ vacancies. The water molecules reside at the intestinal sites 8*c* (1/4, 1/4, 1/4) and 32*f* (*x*, *x*, *x*). The interstitial site 8*c* (1/4, 1/4, 1/4) is denoted by red color as shown in Figure 4. The presence of vacancies and interstitial sites is ideal for hydrogen storage in such compounds.

Figure 5(a) and (b) show EDS analysis spectrum and elemental mapping of the core−shell compound. It is clearly

Table 1. Results of the Rietveld Refinement of Bare−Core $Mn_{1.5}[Cr(CN)_6]\cdot 7.5H_2O$, Bare−Shell $Ni_{1.5}[Cr(CN)_6]\cdot 7.5H_2O$, and Core−Shell Compound $Mn_{1.5}[Cr(CN)_6]\cdot mH_2O$ @$Ni_{1.5}[Cr(CN)_6]\cdot nH_2O$ (*x*′, *y*′, and *z*′ Denote the Fractional Coordinates)

	atom	Wyckoff site	*x*′	*y*′	*z*′	occupancy
bare−core	Mn	4*a*	0	0	0	1
a = 10.8(Å)	Cr	4*b*	0.5	0.5	0.5	0.67
	C	24*e*	0.748(4)	0	0	0.67
	N	24*e*	0.807(1)	0	0	0.67
	O1	24*e*	0.655(9)	0	0	0.35
	O2	32*f*	0.198(3)	0.198(3)	0.198(3)	0.19
	O3	8*c*	0.25	0.25	0.25	0.74
bare−shell	Ni	4*a*	0	0	0	1
a = 10.2(Å)	Cr	4*b*	0.5	0.5	0.5	0.67
	C	24*e*	0.737(1)	0	0	0.67
	N	24*e*	0. 860(6)	0	0	0.67
	O1	24*e*	0.643(6)	0	0	0.35
	O2	32*f*	0.188(4)	0.188(4)	0.188(4)	0.19
	O3	8*c*	0.25	0.25	0.25	0.74
core−shell	Mn	4*a*	0	0	0	0.82
a = 10.5(Å)	Ni	4*a*	0	0	0	0.18
	Cr	4*b*	0.5	0.5	0.5	0.67
	C	24*e*	0.388(9)	0	0	0.67
	N	24*e*	0.679(6)	0	0	0.67
	O1	24*e*	0.679(4)	0	0	0.33
	O2	32*f*	0.35(8)	0.35(8)	0.35(8)	0.1964 (5)
	O3	8*c*	0.25	0.25	0.25	0.73(3)

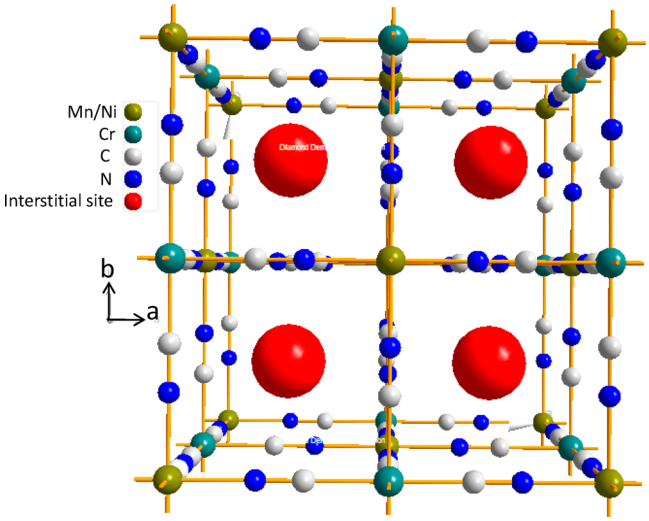

Figure 4. Schematic representation of the unit cell of the core−shell compound. The interstitial site 8*c* (1/4, 1/4, 1/4) is shown by red color in the unit cell.

seen in the EDS spectrum that C, O, N, Cr, Mn and Ni elements are present in the core−shell compound. Moreover, K and Cl are also visible in the spectrum in small concentrations which could be due to unreacted materials used during the sample preparation. Figure 5b shows elemental mapping of core−shell compound. It is observed that the elements C, N, O, Cr, Mn, and, Ni are present and uniformly distributed in the compound.

Figure 6 shows the XPS core level peaks of the metal ions for the core−shell compound. Figures 6a−c represent the core level peaks of the Ni-2p, Cr-2p and Mn-2p, respectively confirming the presence of core and shell elements in the core−shell compound. The peaks are found to be at ∼854.1 eV for Ni 2p3/2, 576.7 eV for Cr-2p3/2 and 641.0 eV for Mn-2p3/2. From the observed binding energy positions of metals ions, it is concluded that the Ni and Mn are in their (+II) valence state, whereas for the case of Cr, it is in (+III) states in the core−shell compound. The satellite peak around ∼860.5 eV has also been seen for the case of Ni-2p peaks. The binding energy positions of ∼641.9 and 642.5 eV are generally observed for Mn(III) and Mn(IV) ions, respectively.

The IR spectra of the bare−core, bare−shell and core−shell compounds are shown in Figure 7a. The characteristic absorption bands for the CN ligands and H_2O molecules are visible for all the compounds. The strong absorption band around ∼3600 cm^{-1} clearly indicates the presence of water

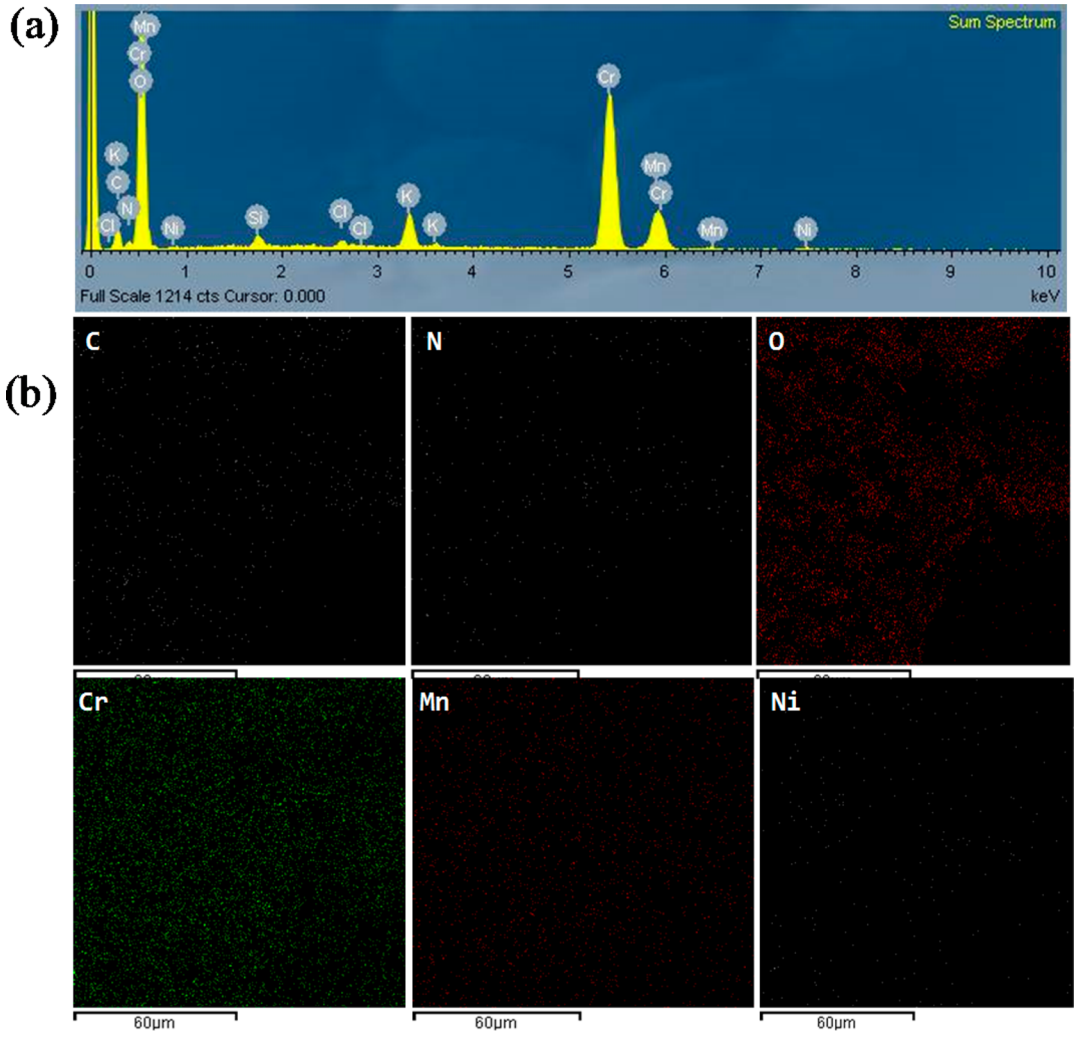

Figure 5. (a) EDS analysis spectrum and (b) elemental mapping of the core−shell compound.

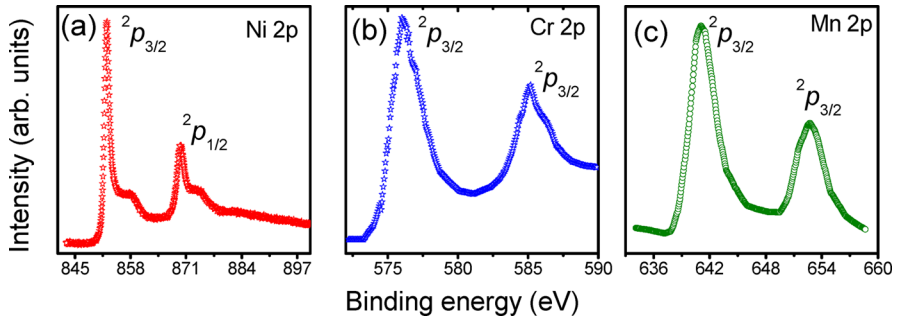

Figure 6. X-ray photoelectron spectroscopy of (a) core level Ni−2p peak, (b) Cr−2p peak, and (c) Mn−2p peak for the core−shell compound.

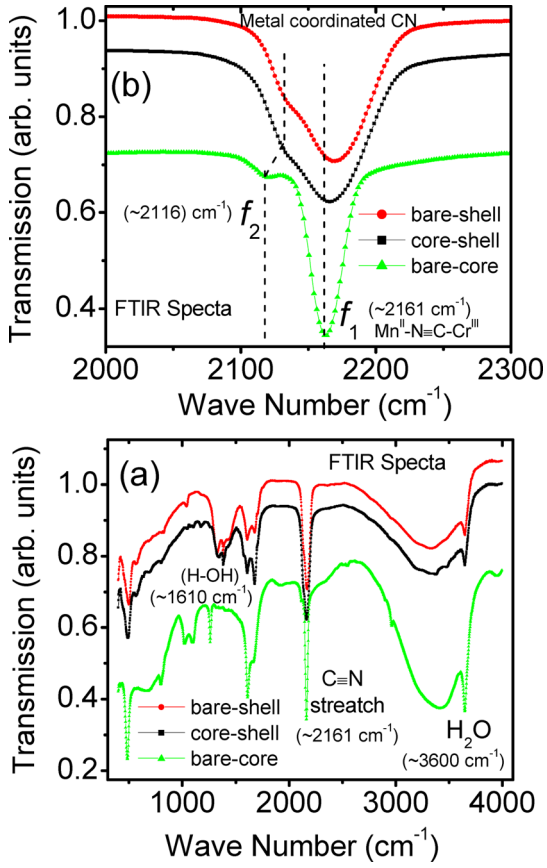

Figure 7. (a) Room-temperature IR transmission spectra for bare−core, bare−shell, and core−shell compounds. (b) IR transmission spectra for CN ligand in the range of 2100−2300 cm^{-1}. Two absorption bands f_1, and f_2 are guided by dotted lines for better visibility. The *y*-axis is shifted for clarity.

molecules in all compounds. The IR spectra in the spectral range of 2000−2300 cm^{-1}, shown in Figure 7b, belong to the stretching frequencies of CN ligand in PBAs. The stretching frequency of the free (CN) molecular ion in an aqueous solution is observed at 2080 cm^{-1}. However, with the formation of the metal cyanide bridge, it is shifted to a higher frequency side. Two absorption bands (f_1 and f_2) are visible for the bare-core compound $Mn_{1.5}[Cr(CN)_6]\cdot 7.5H_2O$. The pronounced band f_1, centered at 2161 cm^{-1} is attributed to the cyanide stretching frequency of $Mn^{II}-N\equiv C-Cr^{III}$. In addition, another absorption band of smaller intensity f_2, centered at 2116 cm^{-1} is attributed due to many reasons. It could be Mn coordinated CN stretching frequency, since Mn ion may possesses different valence states. It is reported that the cyanide coordinated to Mn^{II} has low wavenumber side peak around ∼2125 cm^{-1}, whereas cyanide coordinated to Mn^{III} has a single resolvable high wavenumber peak at ∼2080 cm^{-1}.[40] Moreover, it is also reported that the CN−Mn^{III} stretching modes in different environments in PBAs lie around ∼2114 cm^{-1}.[41] The other possible reason for smaller intensity f_2 peak may be due to potassium ferricyanide, which has the stretching frequency peak at ∼2115 cm^{-1} in solution. This peak may have shifted by about ∼50 cm^{-1} due to the coordination of bond formation in solids.[42] The shoulder peak at ∼2116 cm^{-1} can also be observed when K^+ ion is introduced into the compounds. However, we rule out this possibility as we have not included excess K^+ ions in the compound. Because XPS results do not show the presence of Mn(III) valence state in the compound so IR absorption peak f_2, centered at 2116 cm^{-1} is mainly due to unreacted potassium ferricyanide.

The IR spectrum of the bare−shell compound is similar to that for the bare−core compound, however, broad in nature. The absorption band f_1 for the bare−shell compound $Ni_{1.5}[Cr(CN)_6]\cdot 7.5H_2O$ is observed at ∼2170 cm^{-1}, attributed to the cyanide stretching frequency of $Ni^{II}-N\equiv C-Cr^{III}$. The weak and broad shoulder peak (f_2), centered at ∼2131 cm^{-1} is attributed to $Ni^{II}-C\equiv N-Cr^{III}$ either due to a small fraction of CN flipping in the compound or free cyanide due to an excess of $K_3[Cr(CN)_6]$.[43] The cyanide (N≡C) stretching frequency of $K_3[Cr(CN)_6]$ at ∼2130 cm^{-1} has been previously reported.[44] The CN flipping has been previously reported in many PBAs along with $Ni_{1.5}[Cr(CN)_6]\cdot zH_2O$.[45−49] The IR spectrum of the core−shell compound is similar to that of the bare−shell compound. The absorption band f_1, observed at ∼2165 cm^{-1}, is attributed to the cyanide stretching frequency of $Mn^{II}/Ni^{II}-N\equiv C-Cr^{III}$. The broad weak shoulder peak (f_2), centered at ∼2128 cm^{-1}, may be attributed to nonbridging Cr^{III} −C≡N−, i.e., nitrogen end of the CN ligand is uncoordinated.[45] The values of CN stretching frequencies for all compounds are close to the previously reported CN stretching frequencies of PBAs.[3,50−54] Thus, the characteristic absorption bands of the observed CN stretching frequencies confirm the formation of the PBAs compounds.

Figure 8 shows TGA(a) and DTA(b) spectra of the bare-core, bare-shell, and core−shell compounds recorded in the nitrogen atmosphere. The TGA and DTA figures show that the dehydration temperature for the core−shell compound is the lowest one, whereas, the bare-core compound has highest dehydration temperature. For the core−shell compound, at low temperature, considerable amount of water molecules is present, confirming the porous nature of the structure. During heating, because of the weak binding, the water molecules escape the lattice. The anhydrous phase remains stable up to

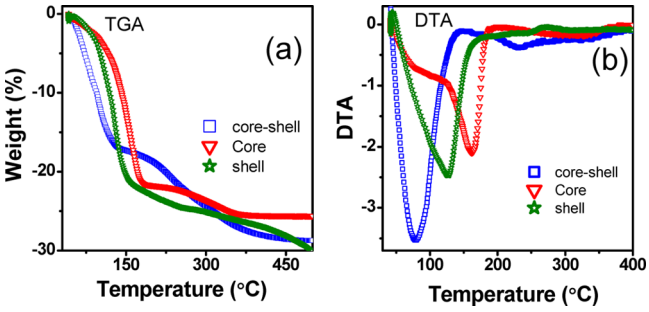

Figure 8. (a) TGA and (b) DTA curves for the core−shell compound.

~175 °C. There is a broad hump in the TGA curve (Figure 8a) around ~150−200 °C for the core−shell compound, suggesting the decomposition for the compound starts at this temperature range. For the bare−core, the water removal temperature is highest, and during the hydrogen adsorption some water molecules are still expected to be present in the porous structure and all the open pores are not available for hydrogen storage. The nature of the bare-shell compound is slightly different. It can be noted from the thermogravimetric data, that there is a continuous weight loss indicating that the noncoordinated and coordinated water molecules are released from the bare−shell compound as the temperature increases. This type of behavior is expected because of the high polarizing power of the Ni metal atom. The number of water molecule released per formula unit at 100 °C has been derived using the present TGA data. It has been found that for the bare−core, bare−shell, and core−shell compounds, they are 2, 3, and 6 water molecules per formula unit.

The hydrogen adsorption isotherms for the bare−core $\{Mn_{1.5}[Cr(CN)_6]\cdot 7.5H_2O\}$, core−shell $\{Mn_{1.5}[Cr(CN)_6]\cdot mH_2O@Ni_{1.5}[Cr(CN)_6]\cdot nH_2O\}$, and bare−shell $\{Ni_{1.5}[Cr(CN)_6\cdot 7.5H_2O]\}$ compounds are shown in Figure 9. The hydrogen adsorption isotherms were obtained by the volumetric method up to a hydrogen pressure of 50 atm. at various temperatures. Significant differences are apparent in the hydrogen adsorption isotherms and the amounts of H_2 adsorbed for all the compounds. For the bare-core compound, the maximum hydrogen storage capacities are found to be 0.14, 0.40, and 0.47 wt % at 300, 273, and 269 K, respectively. The decrease in the storage capacity with increase in the temperature is quite expected as the amount of adsorbed hydrogen depends profoundly on temperature. The hydrogen adsorption data at different temperatures were fitted with the model using the Langmuir expression. From the interpolation of the data, the hydrogen storage capacities at higher pressures also can be found out. It can be seen from the hydrogen adsorption isotherm, that for bare−core compound the hydrogen storage capacity increases almost linearly with increase in the hydrogen pressure. The low adsorption capacity and the nature of the hydrogen adsorption isotherm indicate that all the interstitial spaces are not available for hydrogen adsorption, which has been previously confirmed by the TGA data (Figure 8a).

Thermodynamic parameters, including the Gibb's free energy, enthalpy and the entropy change, provide insights into the adsorption mechanisms, and are important for evaluating the uptake of adsorbents. The apparent isosteric enthalpy of adsorption into the pores of the adsorbent can be calculated conveniently from the Clausiuse Clapeyron equation with the assumption of a model isotherm. The slope of $\ln(p)$ versus $1/T$ at any particular hydrogen coverage gives the heat of hydrogen adsorption. Where p is the equilibrium pressure and T is the temperature of adsorption. The enthalpy of adsorption value decreases with more hydrogen coverage. The enthalpy

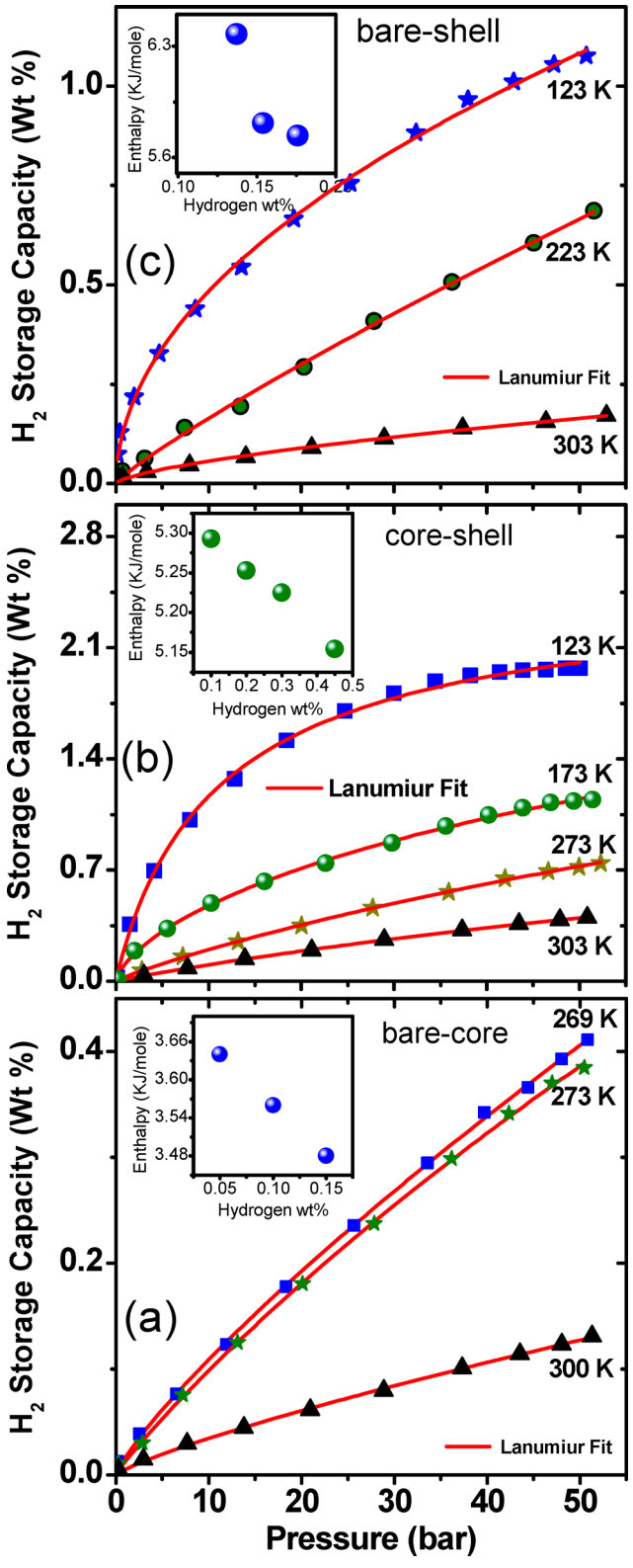

Figure 9. Hydrogen adsorption isotherms of (a) bare−core and (b) core−shell and (c) bare−shell compounds at various temperatures, fitted using Langmuir function. Inset shows the heat of adsorption at different hydrogen storage capacities.

dx.doi.org/10.1021/am503526c | ACS Appl. Mater. Interfaces 2014, 6, 17579−17588

values have been calculated as 3.64, 3.56, and 3.48 kJ/mol, respectively, for 0.05, 0.1, and 0.15 wt % of hydrogen storage capacity for the bare-core compound.

The hydrogen adsorption isotherms for the bare–shell $\{Ni_{1.5}[Cr(CN)_6]\cdot 7.5H_2O\}$, compound are shown in Figure 9c. The hydrogen adsorption isotherm at 50 atm. shows the maximum hydrogen storage of 0.16, 0.68, and 1.09 wt % at 303, 223, and 123 K, respectively. The storage capacity for the bare-shell compound is higher than the bare-core compound. Moreover, the enthalpy of adsorption value has been calculated as 6.37, 5.81, and 5.73 kJ/mol respectively, for 0.1, 0.15, and 0.17 wt % of hydrogen storage capacity for the bare-shell compound.

Figure 9b shows hydrogen adsorption isotherms for the core–shell compound at different temperatures and it shows typical adsorption isotherm indicating stronger interaction between host and the guest. It is interesting to note that the hydrogen storage property for the core–shell compound is significantly improved as compared to the bare-core and bare-shell compounds. The maximum hydrogen storage capacities at various temperatures for the core–shell compound are found to be 0.40, 0.76, 1.14, and 2.0 wt % at 303, 273, 173, and 123 K, respectively. Moreover, the enthalpy of adsorption value for the core–shell compound is higher than the bare–core compound. The enthalpy values for the core–shell compound have been calculated as 5.29, 5.25, 5.22, and 5.15 kJ/mol, respectively, for 0.1, 0.2, 0.3, and 0.45 wt % of hydrogen storage capacity. The enhancement of hydrogen capacity could be due to the fact that the more hydrogen may reside at the interstitial crystallographic sites (1/4, 1/4, 1/4) as well as it may interact with the coordinated unsaturated metal centers. In the literature, it is established that the presence of unsaturated metal sites is responsible for the higher value of enthalpy of adsorption for H_2.[7,55] Figure 10a shows that the PBAs can contain two types of

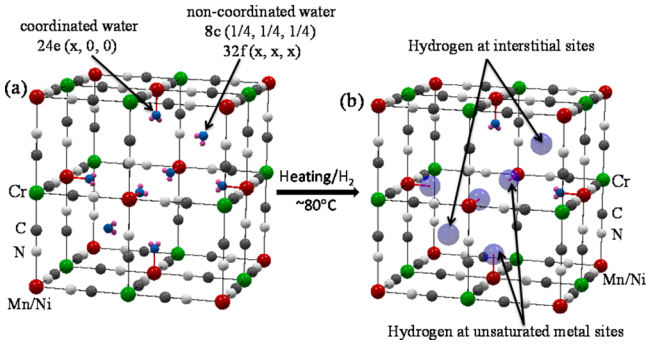

Figure 10. Schematic representation of the unit cell of the core–shell compound showing crystallographic sites for (a) coordinated and noncoordinated water and (b) active sites of hydrogen in the structure of PBAs.

water molecules, i.e., coordinated 24e (x, 0, 0), and noncoordinated (interstitial) 8c (1/4, 1/4, 1/4), and 32f (x, x, x) sites. During the prehydrogen adsorption measurement, the compounds are heated up to ~80 °C. At this temperature, because of the weak binding of the noncoordinated water molecules at 8c and 32f sites, they escape from the lattice, leaving behind the available spaces in the structure for possible hydrogen adsorption. Moreover, at such higher temperatures, apart from the noncoordinated water, some of the coordinated water molecules may also get released, resulting unsaturated metal sites at 24e (x, 0, 0). This unsaturated metal site can also host hydrogen molecules as shown in Figure 10b. From the present TGA and DTA analysis, it is found that the onset of the dehydration temperature for the core–shell compound is the lowest one [~ 70 °C], whereas, the bare-core compound shows the highest (>100 °C) dehydration temperature. Therefore, for the core–shell compound, at ~80 °C, maximum numbers of noncoordinated and coordinated water molecules are expected to get released. Hence, the hydrogen storage capacity decreases from the maximum to minimum in core–shell to bare-shell to bare-core compounds, respectively. However, the neutron diffraction study is underway to ascertain the exact location of the adsorbed hydrogen in the deuterium based core–shell compound. It has been earlier investigated the adsorption of molecular hydrogen in the $Cu_3[Co(CN)_6]_2$ PBAs using high-resolution neutron powder diffraction and neutron vibrational spectroscopy.[56] It was found that the hydrogen was absorbed at two sites within the structure. The most prominent adsorption site, located at the crystallographic site, was an interstitial location within the structure. The second adsorption site was associated with exposed Cu^{2+} ion coordination sites that result from the presence of $[Co(CN)_6]_3$-vacancies within the structure of the material.[56]

We have also studied how the specific surface areas of bare–core, bare–shell, and core–shell compounds are correlated with their hydrogen storage capacity. The specific surface area has been derived using a single point BET (Brunauer–Emmett–Teller) method of nitrogen adsorption isotherm. The method is based on the physical adsorption of nitrogen gas by the sample from a continuously flowing mixture of nitrogen and helium gases, when the sample is cooled to liquid nitrogen temperature. Then the nitrogen gas is left to desorb by raising the temperature of the compounds to 297 K. The change in nitrogen concentration during the adsorption and desorption processes has been monitored by thermal conductivity detector, and the specific surface area has been measured using the following BET equation.[57]

$$\frac{1}{V\left(\frac{P_0}{P}-1\right)} = \frac{1}{V_m C} + \left(\frac{C-P}{V_m C}\right)\left(\frac{P}{P_0}\right)$$

where V is the volume of the adsorption, V_m is the volume of the adsorption for complete monolayer, P_0 is the saturated vapor pressure, P is the equilibrium vapor pressure, and C is the BET constant.

Figure 11 shows N_2 adsorption and desorption spectra of the bare–core, bare–shell, and core–shell compounds at 77 K. All compounds are heated at 80 °C prior to measurements. The values of the specific surface area are found to be maximum for the core–shell (~400 m^2/g), and minimum for the bare-core compounds (~150 m^2/g). The differences in the surface areas are mainly due to the variation of the particle size, unit cell volume, and the stability of the framework structure. Though surface area is not the only criterion for determining the hydrogen storage capacity, but certainly it is important when hydrogen adsorption occurs through physisorption. As the core–shell compound possesses more surface area, better hydrogen storage capacity has been achieved for the core–shell compound compared to the bare–core and bare–shell compounds. The higher and stable surface area in successive experiments for the core–shell compound indicates that the framework structure remains largely stable after heating at 80 °C and also after a few adsorptions-desorption cycles.

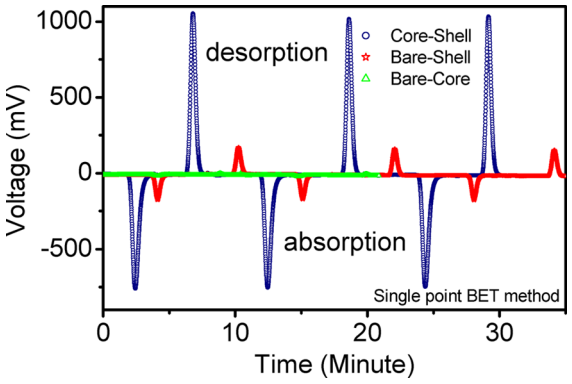

Figure 11. Nitrogen adsorption isotherms of bare–core, bare–shell, and core–shell compounds using BET single point measurements for specific surface area.

The highest H_2 storage capacity is found to be 0.47 wt % at 269 K for bare–core, 1.09 wt % at 123 K for bare-shell, and 2.0 wt % at 123 K for core–shell compounds. These values correspond to 0.94, 2.18, and 4 H_2 molecules per face-centered cubic unit cell for bare-core, bare-shell, and core–shell compound, respectively. The novelty of this work is that we could successfully synthesize core–shell of PBA molecular magnet with an enhanced hydrogen capacity (2.0 wt % at 123 K) as compared to bare–core, bare-shell molecular magnets. To the best of our knowledge, this is the first report on the hydrogen storage properties of any core–shell structure of PBAs with higher storage capacity. The present study could be very useful in the field of hydrogen storage applications.

CONCLUSION

Core–shell PBAs molecular magnet (size ∼25 nm) has been successfully synthesized using a core $Mn_{1.5}[Cr(CN)_6]\cdot 7.5H_2O$, and shell $Ni_{1.5}[Cr(CN)_6]\cdot 7.5H_2O$. The core–shell compound has been extensible studied using TEM, XRD, XPS, IR and TGA measurements. TEM and XRD measurements confirm the core–shell and fcc nature (space group *Fm*3*m*) of the compound. The hydrogen absorption properties of the core–shell compound show an enhancement in the hydrogen adsorption capacity (2.0 wt % at 123 K) as compared to the bare–core and bare–shell compounds. The hydrogen binds at the interstitial [8c (1/4, 1/4, 1/4) and 32 f (*x*, *x*, *x*)] as well as in the coordinated unsaturated metal (Mn/Ni) sites at [24e (*x*, 0, 0)] of the compound. The enhanced hydrogen adsorption capacity is due to higher specific surface area and lowest dehydration temperature of the core–shell compound. We have concluded that the hydrogen storage capacity decreases from maximum in core–shell to minimum in bare–core compound.

AUTHOR INFORMATION

Corresponding Authors

*E-mail: prabhatt@barc.gov.in. Fax: +91 22 25505151.
*E-mail: smyusuf@barc.gov.in.

Notes

The authors declare no competing financial interest.

ACKNOWLEDGMENTS

P.B. thanks Mr. P. Jha for the help in the IR measurement.

REFERENCES

(1) Sato, O.; Iyoda, T.; Fujishima, A.; Hashimoto, K. Photoinduced Magnetization of a Cobalt-Iron Cyanide. *Science* **1996**, *272*, 704–705.
(2) Shimamoto, N.; Ohkoshi, S.; Sato, O.; Hashimoto, K. Control of Charge-Transfer-Induced Spin Transition Temperature on Cobalt–Iron Prussian Blue Analogues. *Inorg. Chem.* **2002**, *41*, 678–684.
(3) Coronado, E.; Giménez-López, M. C.; Korzeniak, T.; Levchenko, G.; Romero, F. M.; Segura, A.; García-Baonza, V.; Cezar, J. C.; Groot, F. M. F. d.; Milner, A.; Paz-Pasternak, M. Pressure-Induced Magnetic Switching and Linkage Isomerism in $K_{0.4}Fe_4[Cr(CN)6]_{2.8}\cdot 16H_2O$: X-ray Absorption and Magnetic Circular Dichroism Studies. *J. Am. Chem. Soc.* **2008**, *130*, 15519–15532.
(4) Ohkoshi, S. I.; Abe, Y.; Fujishima, A.; Hashimoto, K. Design and Preparation of a Novel Magnet Exhibiting Two Compensation Temperatures Based on Molecular Field Theory. *Phys. Rev. Lett.* **1999**, *82*, 1285.
(5) Yusuf, S. M.; Kumar, A.; Yakhmi, J. V. Temperature- and Magnetic-Field-Controlled Magnetic Pole Reversal in a Molecular Magnetic Compound. *Appl. Phys. Lett.* **2009**, *95*, 182506.
(6) Goodwin, A. L.; Chapman, K. W.; Kepert, C. J. Guest-Dependent Negative Thermal Expansion in Nanoporous Prussian Blue Analogues $M^{II}Pt^{IV}(CN)_6\cdot x\{H_2O\}$ ($0 \le x \le 2$; M = Zn, Cd). *J. Am. Chem. Soc.* **2005**, *127*, 17980–17981.
(7) Kaye, S. S.; Long, J. R. Hydrogen Storage in the Dehydrated Prussian Blue Analogues $M_3[Co(CN)_6]_2$ (M = Mn, Fe, Co, Ni, Cu, Zn). *J. Am. Chem. Soc.* **2005**, *127*, 6506–6507.
(8) Coronado, E.; Makarewicz, M.; Prieto-Ruiz, J. P.; Prima-García, H.; Romero, F. M. Magneto-Optical Properties of Electrodeposited Thin Films of the Molecule-Based Magnet Cr5.5 (CN)12 · 11.5H2O. *Adv. Mater.* **2011**, *23*, 4323–4326.
(9) Wessells, C. D.; Huggins, R. A.; Cui, Y. Copper Hexacyanoferrate Battery Electrodes with Long Cycle Life and High Power. *Nat. Commun.* **2011**, *2*, 550.
(10) Lu, Y.; Wang, L.; Cheng, J.; Goodenough, J. B. Prussian Blue: A New Framework of Electrode Materials for Sodium Batteries. *Chem. Commun.* **2012**, *48*, 6544–6546.
(11) Ayrault, S.; Loos-Neskovic, C.; Fredoroff, M.; Garnier, E. Copper Hexacyanoferrates: Preparation, Composition and Structure. *Talanta* **1994**, *41*, 1435–1452.
(12) Hartmann, M.; Grabner, E. W.; Bergveld, P. Alkali Ion Sensor Based on Prussian Blue-Covered Interdigitated Array Electrodes. *Sens. Actuators, B* **1991**, *4*, 333–336.
(13) Koncki, R. Chemical Sensors and Biosensors Based on Prussian Blues. *Crit. Rev. Anal. Chem.* **2002**, *32*, 79–96.
(14) Itaya, K.; Shoji, N.; Uchida, I. Catalysis of the Reduction of Molecular Oxygen to Water at Prussian Blue Modified Electrodes. *J. Am. Chem. Soc.* **1984**, *106*, 3423–3429.
(15) Jena, P. Materials for Hydrogen Storage: Past, Present, and Future. *J. Phys. Chem. Lett.* **2011**, *2*, 206–211.
(16) Sakintuna, B.; Lamari-Darkrim, F.; Hirscher, M. Metal Hydride Materials for Solid Hydrogen Storage: A Review. *Int. J. Hydrogen Energy* **2007**, *32*, 1121–1140.
(17) K.Slattery, D.; Hampton, M. D., Complex Hydrides for Hydrogen Storage. In *Proceedings of the 2002 U.S. DOE Hydrogen Program Review NREL/CP-610–32405*; National Renewable Energy Laboratory: Golden, CO, 2002.
(18) Christian, M. L.; Aguey-Zinsou, K.-F. Core-Shell Strategy Leading to High Reversible Hydrogen Storage Capacity for NaBH4. *ACS Nano* **2012**, *6*, 7739–7751.
(19) Chapman, K. W.; Southon, P. D.; Weeks, C. L.; Kepert, C. J. Reversible Hydrogen Gas Uptake in Nanoporous Prussian Blue Analogues. *Chem. Commun.* **2005**, 3322–3324.
(20) Murray, L. J.; Dinca, M.; Long, J. R. Hydrogen Storage in Metal-Organic Frameworks. *Chem. Soc. Rev.* **2009**, *38*, 1294–1314.
(21) Makowski, P.; Thomas, A.; Kuhn, P.; Goettmann, F. Organic Materials for Hydrogen Storage Applications: From Physisorption on Organic Solids to Chemisorption in Organic Molecules. *Energy Environ. Sci.* **2009**, *2*, 480–490.

(22) Asakura, D.; Li, C. H.; Mizuno, Y.; Okubo, M.; Zhou, H.; Talham, D. R. Bimetallic Cyanide-Bridged Coordination Polymers as Lithium Ion Cathode Materials: Core@Shell Nanoparticles with Enhanced Cyclability. *J. Am. Chem. Soc.* **2013**, *135*, 2793−2799.
(23) Sun, Y. K.; Chen, Z.; Noh, H. J.; Lee, D. J.; Jung, H. G.; Ren, Y.; Wang, S.; Yoon, C. S.; Myung, S. T.; Amine, K. Nanostructured High-Energy Cathode Materials for Advanced Lithium Batteries. *Nat. Mater.* **2012**, *11*, 942−947.
(24) Presle, M.; Lemainque, J.; Guigner, J. M.; Larquet, E.; Maurin, I.; Boilot, J. P.; Gacoin, T. Controlled Growth of Core@Shell Heterostructures Based on Prussian Blue Analogues. *New J. Chem.* **2011**, *35*, 1296−1301.
(25) Okubo, M.; Li, C. H.; Talham, D. R. High Rate Sodium Ion Insertion into Core-Shell Nanoparticles of Prussian Blue Analogues. *Chem. Commun.* **2014**, *50*, 1353−1355.
(26) Dumont, M. F.; Knowles, E. S.; Guiet, A.; Pajerowski, D. M.; Gomez, A.; Kycia, S. W.; Meisel, M. W.; Talham, D. R. Photoinduced Magnetism in Core/Shell Prussian Blue Analogue Heterostructures of $K_jNi_k[Cr(CN)6]_l{\cdot}nH_2O$ with $Rb_aCo_b[Fe(CN)_6]_c{\cdot}m$H2O. *Inorg. Chem.* **2011**, *50*, 4295−4300.
(27) Christian, M.; Aguey-Zinsou, K.-F. Synthesis of Core-Shell NaBH4@M (M = Co, Cu, Fe, Ni, Sn) Nanoparticles Leading to Various Morphologies and Hydrogen Storage Properties. *Chem. Commun.* **2013**, *49*, 6794−6796.
(28) Reguera, L.; Balmaseda, J.; Krap, C. P.; Avila, M.; Reguera, E. Hydrogen Storage in Zeolite-Like Hexacyanometallates: Role of the Building Block. *J. Phys. Chem. C* **2008**, *112*, 17443−17449.
(29) Reguera, L.; Krap, C. P.; Balmaseda, J.; Reguera, E. Hydrogen Storage in Copper Prussian Blue Analogues: Evidence of H2 Coordination to the Copper Atom. *J. Phys. Chem. C* **2008**, *112*, 15893−15899.
(30) Reguera, L.; Balmaseda, J.; del Castillo, L. F.; Reguera, E. Hydrogen Storage in Porous Cyanometalates: Role of the Exchangeable Alkali Metal. *J. Phys. Chem. C* **2008**, *112*, 5589−5597.
(31) Reguera, L.; Balmaseda, J.; Krap, C. P.; Reguera, E. Hydrogen Storage in Porous Transition Metals Nitroprussides. *J. Phys. Chem. C* **2008**, *112*, 10490−10501.
(32) Kaye, S. S.; Long, J. R. The Role of Vacancies in the Hydrogen Storage Properties of Prussian Blue Analogues. *Catal. Today* **2007**, *120*, 311−316.
(33) Krap, C. P.; Balmaseda, J.; Zamora, B.; Reguera, E. Hydrogen Storage in the Iron Series of Porous Prussian Blue Analogues. *Int. J. Hydrogen Energy* **2010**, *35*, 10381−10386.
(34) Kaye, S. S.; Long, J. R. Hydrogen Adsorption in Dehydrated Variants of the Cyano-Bridged Framework Compounds $A_2Zn_3[Fe(CN)_6]_2{\cdot}xH_2O$ (A = H, Li, Na, K, Rb). *Chem. Commun.* **2007**, 4486−4488.
(35) Yang, D.; Ding, V.; Luo, J.; Currier, R.; Obrey, S.; Zhao, Y., Hydrogen Adsorption in Thin Films of Prussian Blue Analogues. *Conference Procedings: American Institute of Chemical Engineers* 2008, AIChE Annual Meeting Phiadelphia: PA.
(36) Brinzei, D.; Catala, L.; Louvain, N.; Rogez, G.; Stephan, O.; Gloter, A.; Mallah, T. Spontaneous Stabilization and Isolation of Dispersible Bimetallic Coordination Nanoparticles of CsxNi[Cr(CN)-6]y. *J. Mater. Chem.* **2006**, *16*, 2593−2599.
(37) Catala, L.; Brinzei, D.; Prado, Y.; Gloter, A.; Stéphan, O.; Rogez, G.; Mallah, T. Core−Multishell Magnetic Coordination Nanoparticles: Toward Multifunctionality on the Nanoscale. *Angew. Chem., Int. Ed.* **2009**, *48*, 183−187.
(38) Rodriguez-Carvajal, J. *FULLPROF, November* 2007, website: http://www.ill.eu/sites/fullprof/.
(39) Rietveld, H. M. A Profile Refinement Method for Nuclear and Magnetic Structures. *J. Appl. Crystallogr.* **1969**, *2*, 65−71.
(40) Phu; Kim, P.; Thuan; Minh, N.; Minh, V.; Nguyen. Synthesis, Characterisation and Structural Studies of $Rb_xMn[Fe(CN)_6]$. *J. Exp. Nanosci.* **2012**, *7*, 336−343.
(41) Lummen, T. T. A.; Gengler, R. Y. N.; Rudolf, P.; Lusitani, F.; Vertelman, E. J. M.; van Koningsbruggen, P. J.; Knupfer, M.; Molodtsova, O.; Pireaux, J. J.; van Loosdrecht, P. H. M. Bulk and Surface Switching in Mnâ'Fe-Based Prussian Blue Analogues. *J. Phys. Chem. C* **2008**, *112*, 14158−14167.
(42) Martinez-Garcia, R.; Knobel, M.; Reguera, E. Modification of the Magnetic Properties in Molecular Magnets Based on Prussian Blue Analogues Through Adsorbed Species. *J. Phys.: Condens. Matter* **2006**, *18*, 11243.
(43) León, M. C.; Coronado, E.; Muñoz, Á. L.; Repetto, D.; Mingotaud, C.; Brinzei, D.; Catala, L.; Mallah, T. Magnetic Langmuir−Blodgett Films of Bimetallic Coordination Nanoparticles of $Cs_{0.4}Ni[Cr(CN)_6]_{0.9}$. *Chem. Mater.* **2008**, *20*, 4642−4652.
(44) Nakamoto, K. *Infrared and Raman Spectra of Inorganic andCoordination Compounds*, 3rd ed., Wiley, New York, 1978.
(45) Yusuf, S. M.; Thakur, N.; Kumar, A.; Yakhmi, J. V. Cyanide-Bridged $Ru_xNi_{3-3x/2}[Cr(CN)_6]_2{\cdot}zH_2O$ Molecular Magnets:Controlling Structural Disorder and Magnetic Properties by a 4d Ion (Ruthenium) Substitution. *J. Appl. Phys.* **2010**, *107*, 053902.
(46) Kumar, A.; Yusuf, S. M.; Keller, L.; Yakhmi, J. V.; Srivastava, J. K.; Paulose, P. L. Variation of Structural and Magnetic Properties with Composition in the $(Co_xNi_{1-x})_{1.5}[Fe(CN)_6]{\cdot}zH_2O$ Series. *Phys. Rev. B* **2007**, *75*, 224419.
(47) Kumar, A.; Yusuf, S. M.; Keller, L.; Yakhmi, J. V. Microscopic Understanding of Negative Magnetization in Cu, Mn, and Fe Based Prussian Blue Analogues. *Phys. Rev. Lett.* **2008**, *101*, 207206.
(48) Brown, D. B.; Shriver, D. F.; Schwartz, L. H. Solid- State Reactions of Iron(II) Hexacyanochromate(III). *Inorg. Chem.* **1968**, *7*, 77−83.
(49) Nakamoto, K. *Infrared and Raman Spectra of Inorganic and Coordination Compounds, Part B: Applications in Coordination, Organometallic and Bioinorganic Chemistry*, 5th ed.; Wiley-Interscience: New York, 1997.
(50) Arai, M.; Miyake, M.; Yamada, M. Metal(II) Hexacyanochromate(III) MCr (M = Co, Cu, Fe) Coordination Nanoparticles Stabilized by Alkyl Surface Coordination Ligand: Downsizing Effect on Their Crystal Structure and Magnetic Properties. *J. Phys. Chem. C* **2008**, *112*, 1953−1962.
(51) Kosaka, W.; Nomura, K.; Hashimoto, K.; Ohkoshi, S. Observation of an Fe(II) Spin-Crossover in a Cesium Iron Hexacyanochromate. *J. Am. Chem. Soc.* **2005**, *127*, 8590−8591.
(52) Shriver, D. F.; Shriver, S. A.; Anderson, S. E. Ligand Field Strength of the Nitrogen End of Cyanide and Structures of Cubic Cyanide Polymers. *Inorg. Chem.* **1965**, *4*, 725.
(53) Nuida, T.; Matsuda, T.; Tokoro, H.; Sakurai, S.; Hashimoto, K.; Ohkoshi, S.-i. Nonlinear Magnetooptical Effects Caused by Piezoelectric Ferromagnetism in $F\bar{4}3m$-type Prussian Blue Analogues. *J. Am. Chem. Soc.* **2005**, *127*, 11604.
(54) Ohkoshi, S.-i.; Hashimoto, K. Ferromagnetism of Cobalt-Chromium Polycyanides. *Chem. Phys. Lett.* **1999**, *314*, 210−214.
(55) Hazra, A.; Kanoo, P.; Maji, T. K. High Heat of Hydrogen Adsorption and Guest-Responsive Magnetic Modulation in a 3D Porous Pillared-Layer Coordination Framework. *Chem.Commun.* **2011**, *47*, 538−540.
(56) Hartman, M. R.; Peterson, V. K.; Liu, Y.; Kaye, S. S.; Long, J. R. Neutron Diffraction and Neutron Vibrational Spectroscopy Studies of Hydrogen Adsorption in the Prussian Blue Analogue $Cu_3[Co(CN)_6]_2$. *Chem. Mater.* **2006**, *18*, 3221−3224.
(57) Brunauer, S.; Emmett, P. H.; Teller, E. Adsorption of Gases in Multimolecular Layers. *J. Am. Chem. Soc.* **1938**, *60*, 309−319.